The final publication is available at

https://doi.org/10.1016/j.jelechem.2021.115366

Additional Information

Organophosphorus pesticides (chlorfenvinphos, phosmet and fenamiphos) photoelectrodegradation by using WO₃ nanostructures as photoanode.

Gemma Roselló-Márquez,[a] Ramón Manuel Fernández-Domene,[b] José García-Antón[a]

[a] *Ingeniería Electroquímica y Corrosión, Instituto Unversitario de Seguridad Industrial, Radiofísica y Medioambiental, Universitat Politècnica de València, C/Camino de Vera s/n, 46022, Valencia, Spain*

[b] *Departmento de Ingeniería Química, Universitat de Valencia, Av de les Universitats, s/n, 46100, Burjassot, Spain*

jgarciaa@iqn.upv.es

Abstract

The photoelectrocatalytic (PEC) degradation of recalcitrant and toxic organophosphorus pesticides, fenamiphos, chlorfenvinphos and phosmet, has been performed by using an innovative WO₃ nanostructure as photoanode. The nanostructure has been synthesized by anodization in acidic media in the presence of a very small amount (0.05 M) of H_2O_2, and its composition as well as its photoelectrochemical properties have been characterized using X-ray Photoelectron Spectroscopy and X-ray diffraction as composition technique and photoelectrochemical impedance spectroscopy as photoelectrochemical analysis. After 24 hours of experiment, a degradation of 95% of chlorfenvinphos, 99.9% of phosmet and 100% of fenamiphos has been achieved following pseudo-first order kinetics, indicating the good PEC efficiency of this WO₃ nanostructure. Moreover, different intermediates have been identified by means of Ultra-High Performance Liquid Chromatograph coupled to a Time of Flight and

Mass Spectrometer (UHPLC-Q-TOF/MS) for each of the pesticides after 24 hours of photoelectrocatalytic degradation. With these identified compounds, a degradation route has been proposed for each of the pesticides in which they are decomposed into other smaller and less toxic molecules.

Keywords: WO$_3$ nanostructures, degradation, UHPLC-Q-TOF/MS, pesticides, photoelectrocatalysis.

1. Introduction.

Organophosphorus pesticides (OP) have become one of the most widely used groups of chemical insecticides for pest control but include some of the most toxic pesticides used in agriculture [1]. They are characterized by having high toxicity for fish and aquatic invertebrates producing the inhibition of acetylcholinesterase activity. In this type of poisoning, there are signs and symptoms corresponding to manifestations that are classified into three types: muscarinic, nicotinic, and of the central nervous system (CNS) [2]. Additionally, organophosphorus compounds can cause water contamination and damage to plants or animals that were not the target of the pesticide application. Moreover, due to their intensive use in agriculture, high levels of these products are found in groundwater and surface waters. In addition, the repeated application of a pesticide in the same place can often influence the activities of soil microorganisms responsible for its biodegradation, causing a greater accumulation of the pesticide [3]. The three organophosphorus pesticides studied in this work have been phosmet, fenamiphos and chlorfenvinphos, which are among the most widely used worldwide.

Since crop pesticides end up in natural waters, effective and rapid disposal methods are needed. In order to decontaminate wastewater that contains toxic organic matter, many techniques are used such as activated carbon adsorption, ozonation or biodegradation. Among these, Advanced Oxidation Processes (AOP) have been successfully applied to degrade organic

compounds present in contaminated water. In AOP, hydroxyl radicals (HO·) are used as an oxidizing agent to degrade organic pollutants. These radicals are very interesting due to their high oxidation efficiency and their non-selective reactivity [4,5].

This can be achieved by photoelectrocatalytic (PEC) technology, which is based on electrochemical devices using nanostructured materials based on n-type metal oxides. Among these, tungsten oxide (WO_3) has exceptional properties, such as suitable bandgap, high electron mobility, low cost and very good surface stability.

Various techniques have been used to obtain nanostructures, such as sputtering, chemical vapor deposition, sol-gel, hydrothermal methods and electrochemical anodization. The last one is a good option since it is a simple and low cost method, easy to control its parameters and increases the surface-volume ratio. Often, post-anodization treatment is required to further increase the crystallinity of WO_3 nanostructures to improve their PEC performance.

So, in the present study, there are two objectives. The first one is to characterize both structurally and photoelectrochemically the WO_3 nanostructures used as photoelectrocatalysis obtained in three different electrolytes (H_2SO_4, CH_4O_3S and HNO_3). Then, the second objective of this study is to degrade the three pesticides described above with the nanostructure that presents better characteristics and properties by photoelectrocatalysis. The monitoring and identification of possible intermediates will be followed by UHPLC-Q-TOF/MS.

2. Experimental procedure.

2.1. Synthesis of WO_3 nanostructures

On the one hand, WO_3 nanostructures were obtained by electrochemical anodization in a 2-electrode cell with a tungsten rod anode and a platinum mesh cathode. Previously to anodization, the tungsten rod surface was polished with 240–4000 SiC papers to achieve a mirror finish. Then, a deep cleaning of the surface was carried out by sonication in ethanol for

2 min. Anodization was performed in three different electrolytes, with H_2O_2 0.05 M in all of them. The first one was sulfuric acid (H_2SO_4) 1.5 M. The second one was nitric acid (HNO_3) 1.5 M, and finally, the third one was methanesulfonic acid (CH_4O_3S) 1.5 M. During the process, current density versus time was recorded. Finally, the anodized samples were annealed at 600 $^\circ$C for 4 hour in air atmosphere.

2.2. Structural characterization (XRD and XPS)

The crystalline structure of the samples was analyzed by X-ray diffraction (XRD) analysis using an D8AVANCE diffractometer (Bruker) equipped with a monochromatic Cu Kα1 source. Moreover, the electronic states of the nucleus and of the valence of WO_3 nanostructures were analyzed through X-ray photoelectron spectroscopy (XPS, K-ALPHA, Thermo Scientific). Al-K_ radiation (1486.6 eV) monochromatized by a twin crystal monochromator providing a focused X-ray spot at 3 mA × 12 kV was employed to collect the spectra. The alpha hemispherical analyzer operated in the constant energy mode by using 200 eV survey scan pass energies for the whole energy band measurements and 50 eV in a narrow scan for the elements. The experimental backgrounds were approximated by using a smart background function and from background-substracted peak areas surface elemental composition were calculated. The system flood gun yielding from a single source low energy electrons and low energy argon ions provided the charge compensation.

2.3. Photoelectrochemical characterization

A photoelectrochemical characterization was carried out to the nanostructures that presented better structural properties (synthetized in CH_4O_3S). With the aim of evaluating whether the charge transfer of holes occurs directly from the valence band or indirectly via surface states, the interfacial charge transfer capacitance (C_2) versus the applied potential was studied. All these experiments were performed in a three-electrode configuration cell with 0.1 M H_2SO_4 as electrolyte. The WO_3 samples were used as working electrode, a platinum foil as the counter-

electrode and an Ag/AgCl electrode as the reference electrode. The electrodes were immersed in the electrolyte and connected to a potentiostat (Autolab). The applied potential varied between 0.3 V and 1 V with steps of 100 mV and simulated sunlight conditions were achieved using AM 1.5 illumination.

2.4. Photoelectrocatalytic degradation

For the photoelectrocatalytic (PEC) degradation experiments, a 500 W xenon lamp was employed as the visible light source to carry out the experiments under illumination conditions. The distance between the photoreactor and lamp was 30 cm and the visible light intensity was 100 mW/cm^2. The degradation of the pesticides under visible light irradiation was carried out in a quartz reactor with nanostructures acting as the photoanode, a platinum wire serving as the counter electrode, and a Ag/AgCl 3 M KCl electrode performing as the reference electrode. The bias potential applied to the photoanode was 1 V (vs Ag/AgCl). All the experiments were performed with magnetic stirring at room temperature.


2.5. UHPLC-Q-TOF/MS analysis.

Chromatographic analysis was carried out using an Agilent 1290 Infinity UHPLC system equipped with a C-18 analytical column (Agilent ZORBAX Eclipse Plus C18, 50 mm × 2.1 mm, 1.8 m particle size). 20 μL of the sample extract was injected in each run. Mobile phases A and B were mili-Q water and acetonitrile, both with 0.1% (v/v) acetic acid. The chromatographic method used an initial mobile phase composition of 5% of B constant for 3 min. Then, this composition augmented until 10% of B, an finally, it was followed by a linear gradient to 100% B up to 25 min, and kept for 3 min at 100% B. The flow rate was 0.5 mL min^{-1}. The UHPLC system was connected to a time-of flight (TOF) mass spectrometer equipped with an electrospray interface operated in positive or negative ionization mode, using the following operation parameters: capillary voltage 4000 V; nebulizer pressure 40 psi; drying gas flowrate

9 L min^{-1}; gas temperature 325°C; skimmer voltage 65 V; octopole rf 250 V; fragmentor voltage 190 V. LC–MS accurate mass spectra were recorded across the range of 70–1200 m/z in positive ionization mode.

3. Results and discussion.

3.1. X-ray diffraction (XRD).

The XRD patterns of the WO$_3$ nanostructures synthesized in different electrolytes are shown in Figure 1. All the peaks in the XRD patterns correspond to the monoclinic structure of polycrystalline WO$_3$. Moreover, FE-SEM images of three samples are shown in inset of Figure 1, where it can be seen in all cases a nanorod morphology.
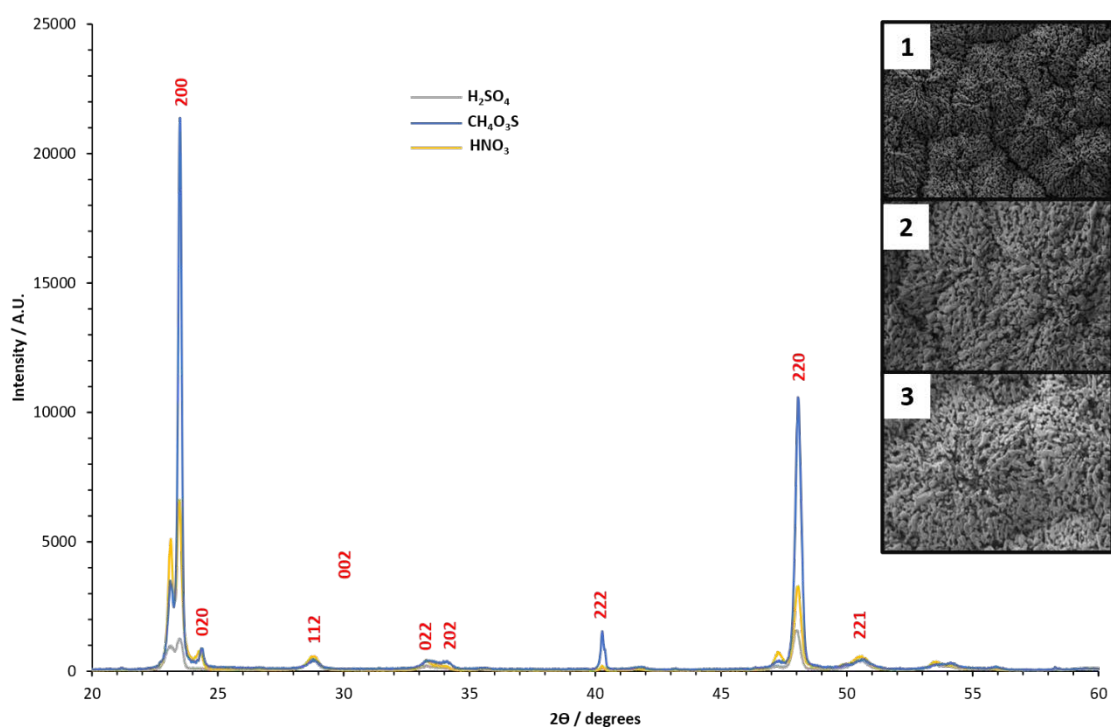
Figure 1. XRD patterns of WO$_3$ nanostructures synthesized with H$_2$SO$_4$, CH$_4$O$_3$S and HNO$_3$ as electrolyte. Insets show FE-SEM images of nanostructures obtain with 1) H$_2$SO$_4$, 2) CH$_4$O$_3$S and 3) HNO$_3$.

After annealing at 600°C during 4 hours, in the three different samples, strong and sharp diffraction peaks are observed at 2θ = 23.15°,23.48°, 24.25°, 28.75°, 33.35°, 34.27°,40.3°, 48.05°, 50.52° are associated to the (002), (200), (020), (112), (022), (202), (222), (220) and

6

(221) crystalline planes of the monoclinic phase of WO_3 with good crystallization. The predominance of triplet (002), (020) and (200) [14,15] in the patterns establishes the monoclinic phase of the prepared samples. Moreover, it has been observed that the use of CH_4O_3S as electrolyte led to a considerable improvement in the crystallinity since the peaks are more intense and defined. Such improvement in peak intensity may be related to the number of grains oriented along these planes, and also to the improved crystallinity of the material [16].

Furthermore, the crystallites size is one of the critical parameters that influences the metal oxide nanostructures properties, which is calculated by using Scherrer's equation (eq 1).

$$D = \frac{k\lambda}{FWHM \cdot cos\theta} \qquad (eq.1)$$

where D is the crystallite size, k is a shape factor (0.9), λ is the X-ray wavelength (0.15406 nm), $FWHM$ is the full width at half maximum intensity in radians and θ is the Bragg angle [17,18]. The average crystallite sizes calculated along the main principal peak (002), (020) and (200) of the three samples analyzed are shown in the Table S1.

The decrease in crystalline-size could be suitable for transfer of photogenerated charge-carriers to the surface of catalyst where it might play substantial role to improve photocatalytic performance through decreasing the recombination rate of charge-carriers [19,20]. This decrease in size is reflected in the nanostructures synthesized in CH_4O_3S as electrolyte, where the size of the crystals in any of the crystallographic planes is smaller than in the other two samples.

3.2. Surface characterization of nanostructures by X-ray Photoelectron Spectroscopy (XPS).

In order to obtain qualitative and quantitative information on all the elements present in the nanostructures an X-ray Photoelectron Spectroscopy (XPS) analysis has been carried out. The samples analysed were three samples synthesized with three different electrolytes (H_2SO_4,

CH_4O_3S and HNO_3) and later annealed in air at 600 °C since these were the optimal annealing conditions. In this technique, an analysis of the electronic states of the nucleus and of the valence (bonding electrons) is carried out, which provides information on the chemical nature of the samples.

The elements present in the nanostructures of the three samples are tungsten, oxygen and nitrogen. Next, a quantitative comparison of these elements will be made in the samples analyzed.

3.2.1. Tungsten.

The first element detected in the XPS spectrum of the three samples was tungsten. Figure 2 a, b and c show the XPS spectra of the peaks associated with tungsten for the samples synthesized in H_2SO_4, CH_4O_3S and HNO_3 respectively. In all three cases, two main peaks can be observed, such as $W4f_{7/2}$ and $W4f_{5/2}$ (in black). Furthermore, these peaks can be deconvoluted in order to obtain independent peaks that are associated with different states of tungsten. In this case, the deconvolution of the $W4f_{7/2}$ peak will be carried out, since it is the one selected according to the bibliography. When performing the deconvolution of $W4f_{7/2}$, three peaks associated with W were observed. The peaks appear at 34.6 eV ($W4f_{7/2}$ Scan A, blue in all three graphs), 35.5 eV ($W4f_{7/2}$ Scan B, orange in all three graphs) and 36.4 eV ($W4f_{7/2}$ Scan C, green in all three graphs). The peak associated with the generation of photoelectrons emitted by W atoms with oxidation state +6 (WO_3), that is, when stoichiometric tungsten oxide is present, is the second peak ($W4f_{7/2}$ Scan B), which appears at 35.5 eV [21]. Instead, the first and third peaks are associated with vacancies or defects in the nanostructures. The first one ($W4f_{7/2}$ Scan A) refers to the photoelectrons emitted by the tungsten atoms near the oxygen vacancies, where the oxidation state of W is less than +6 (substoichiometric WO_{3-x}). Finally, the third peak ($W4f_{7/2}$ Scan C), is associated with local variations in the energy of the vacuum level (E_{vl}) caused by surface defects.

8

After analyzing the three graphs together, it can be observed that the peak associated with W^{+6} (W4f$_{7/2}$ Scan B), and therefore with the stoichiometric tungsten oxide, presents greater intensity and greater area in the case of the sample synthesized with H_2SO_4, followed by the sample anodized with HNO_3, and finally, those with the lowest intensity are those of the sample synthesized with CH_4O_3S. The lower the intensity of the peaks, the lower the amount of W^{+6}, and therefore, the greater amount of non-stochiometric tungsten oxide (WO_{3-x}) will be found, resulting in a greater amount of vacancies in the structure.

In addition, this finding is confirmed by analyzing the data obtained from the peak associated with oxygen vacancies (W4f$_{7/2}$ Scan A), since the peak with the highest intensity is that of the sample obtained with CH_4O_3S, followed by that of the sample synthesized in HNO_3 and finally the one with the lowest intensity is the one obtained in H_2SO_4. Therefore, by analyzing both peaks, it can be stated that the sample with the greatest amount of oxygen vacancies is the one synthesized in CH_4O_3S.

Finally, if the peak associated with surface defects (W4f$_{7/2}$ Scan C) is analyzed, it can be concluded that the sample with the highest density of surface defects is the one synthesized in HNO_3, followed by the sample synthesized in H_2SO_4, and finally the one that less density of superficial defects is obtained in CH_4O_3S. This result can be associated with the incorporation of the nitrogen present in the electrolyte, resulting in nitrogen-doped nanostructures. In addition, this effect will also be reflected in the peaks associated with oxygen.
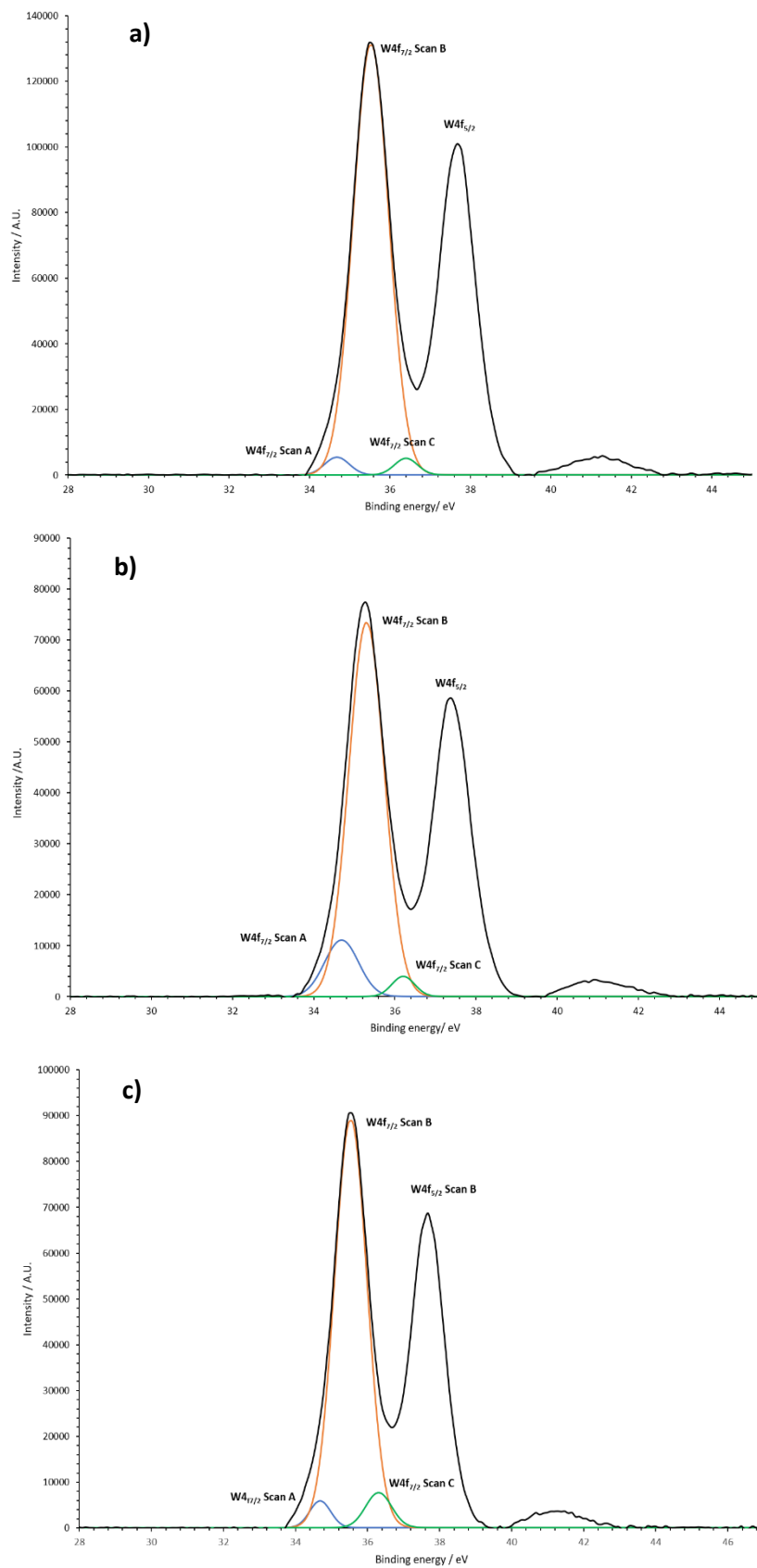
Figure 2. High resolution XPS spectra of peak W4f of the samples synthesized with a) H_2SO_4, b) CH_4O_3S and c) HNO_3.

Table S2 shows the normalized area of the $W4f_{7/2}$ peak of the three samples, where it is verified that the $W4f_{7/2}$ Scan B peak of the sample anodized in CH_4O_3S presents a smaller area and therefore, a lower amount of W in state oxidation +6, resulting in a greater number of vacancies in its structure.

3.2.2. Oxygen

Another element detected in the XPS analysis of the three samples was oxygen. Figure 3 a, b and c show the results of the deconvolution (decomposition into three peaks) of the O1s line for the tungsten oxide samples synthesized in H_2SO_4, CH_4O_3S and HNO_3. In all three cases, the shape of the spectra is similar, with three differentiated peaks.

The peak that appears at a binding energy of 529.92 eV (O1s Scan A) corresponds to the oxygen atoms O^{2-} in the lattice, however, the peaks that appear at a binding energy of 531.5 (O1s Scan B) and 532.9 eV (O1s Scan C) are related to defects in nanostructures. The first of them is associated with hydroxyl groups (-OH) present on the surface of the samples, while the second of them is related to the adsorbed species and oxygen atoms in the O^- state, that is, oxygen vacancies [22,23].

The increased content of -OH groups on the surface of non-stoichiometric tungsten oxides can be explained by the possibility of filling oxygen vacancies by the -OH group. In that case, the W^{5+} cation must be in the center of the octahedron of five O^{2-} ions and one OH− anion.

In addition, according to Shpak research [22], a direct connexion is shown between the catalytic and electrochemical activity of compounds with hydroxyl groups, leading to better catalytic behaviors as the amount of hydroxyl groups increases.

Once it is explained what each peak corresponds to, the spectra of the three studied samples will be analyzed.

The peak associated with the oxygen atoms O^{2-} in the lattice (529.92 eV) is higher in the sample synthesized in H_2SO_4, followed by the sample synthesized in HNO_3, and finally, the sample with a lower peak is the one synthesized in CH_4O_3S, indicating that it is the sample with the higher amount of oxygen vacancies, since it has a lower density of oxygen atoms O^{2-} in the network.

Furthermore, if the two remaining peaks are analyzed, it can be concluded that the sample synthesized in CH_4O_3S presents a greater amount of oxygen vacancies since the peak associated with these vacancies (O1s Scan C) is greater than that of the rest of the samples. Finally, when comparing the second peak (O1s Scan B) it can be observed that the one with the greatest area (as observed in Table S3) and intensity is the one obtained with the sample synthesized in HNO_3, indicating that it has a greater amount of -OH group on the surface and therefore greater surface defects, as predicted when analyzing the peak of tungsten $W4f_{7/2}$ Scan C. The second sample with greater intensity in this peak is the one synthesized in CH_4O_3S being the one with the smallest area the one synthesized in H_2SO_4.
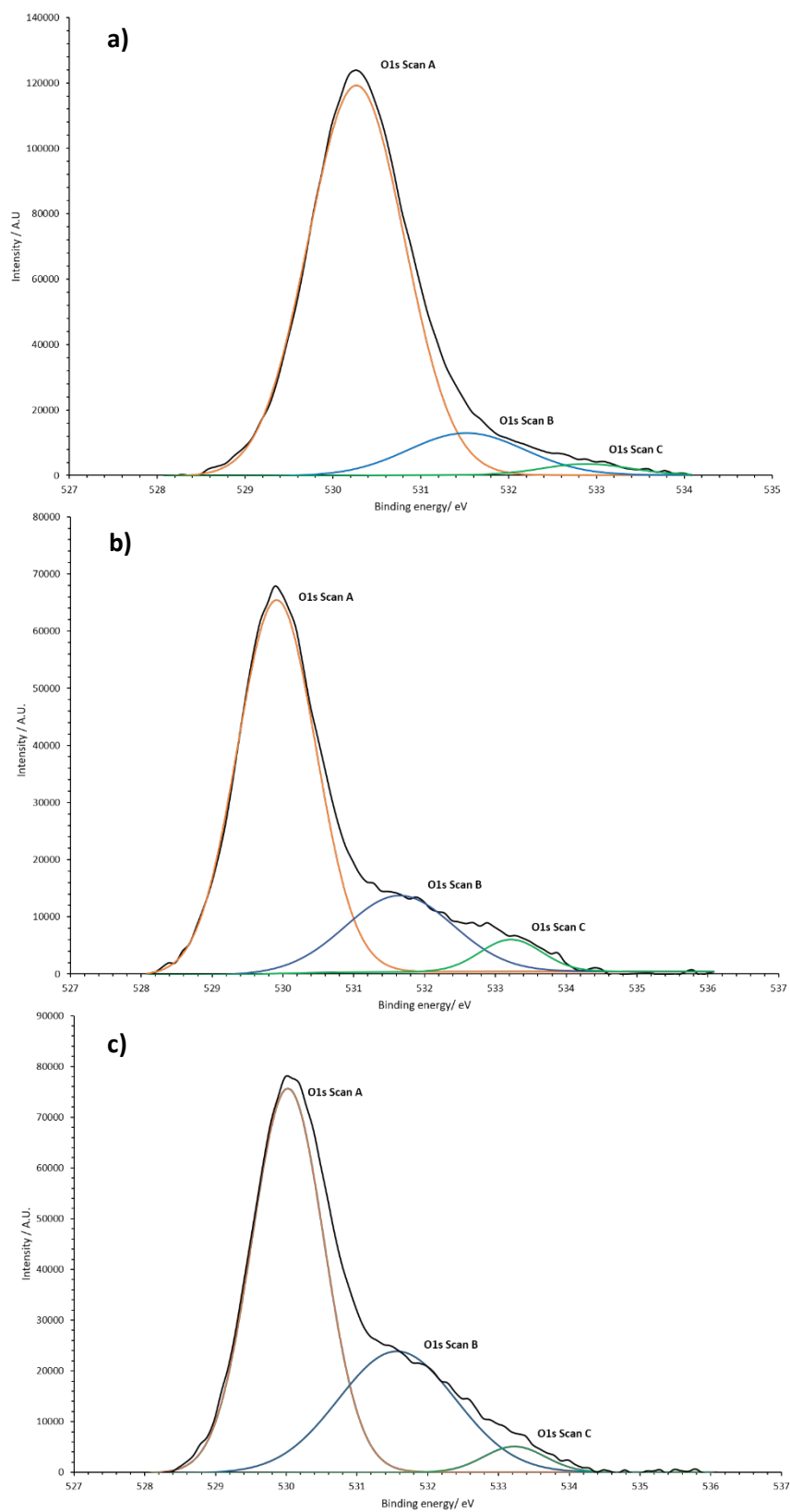
Figure 3. High resolution XPS spectra of O1s peak of samples synthesized with a) H_2SO_4 b) CH_4O_3S and c) HNO_3.

3.2.3. Nitrogen

The third and last element identified in the XPS analysis was nitrogen, but unlike the other two elements, it was only detected in samples synthesized in CH_4O_3S and HNO_3. Figure 4 a and b shows deconvolution results (decomposition into three peaks) of the N1s line for the tungsten oxide samples synthesized in CH_4O_3S and HNO_3.

Theoretically, the spectrum associated with nitrogen N1s is separated into three different peaks, but in the case of the sample synthesized in CH_4O_3S only the first appears, while in the spectrum of the sample synthesized with HNO_3 the first and the second appear, being the third practically negligible.

The first peak appears around 399.4 eV and the second at 401.02 eV. Both peaks indicate the presence of nitrogen in the nanostructures, but in a different way. Although the peak at 399.4 eV corresponds to nitrogen bound to tungsten oxide, indicating the presence of nitrogen in the films, the second peak centered at 401.7 eV corresponds to nitrogen adsorbed on the surface and nitrogen trapped in the surface layers as N_2 [24,25].

Analyzing the spectra obtained for both samples, it can be concluded that the nanostructures with the highest nitrogen concentration are those obtained in HNO_3, followed by the sample obtained in CH_4O_3S, and finally the one obtained in H_2SO_4, which do not present nitrogen in the structure (as observed in Table S4). This is mainly due to the effect of the electrolyte used in the synthesis of the nanostructures since when anodizing in HNO_3, nitrogen is incorporated into the network, forming W-O-N. In addition, the fact that the second sample with the highest nitrogen content is the one synthesized in CH_4O_3S is logical since it is the sample with the greatest number of defects (as seen above) and causes the nitrogen present in the atmosphere (due to the samples submitted to heat treatment in air) is easier to incorporate into the network than in the case of the sample synthesized in H_2SO_4, which has fewer defects.

In addition, the fact that the second peak only appears in the spectrum of the sample synthesized in HNO$_3$ is coherent since the adsorption of nitrogen compounds on the surface is mainly due to the electrolyte used, which contains nitrogen, and therefore, this peak does not appear in the other two samples since the electrolytes used in their synthesis do not contain nitrogen in their structure.
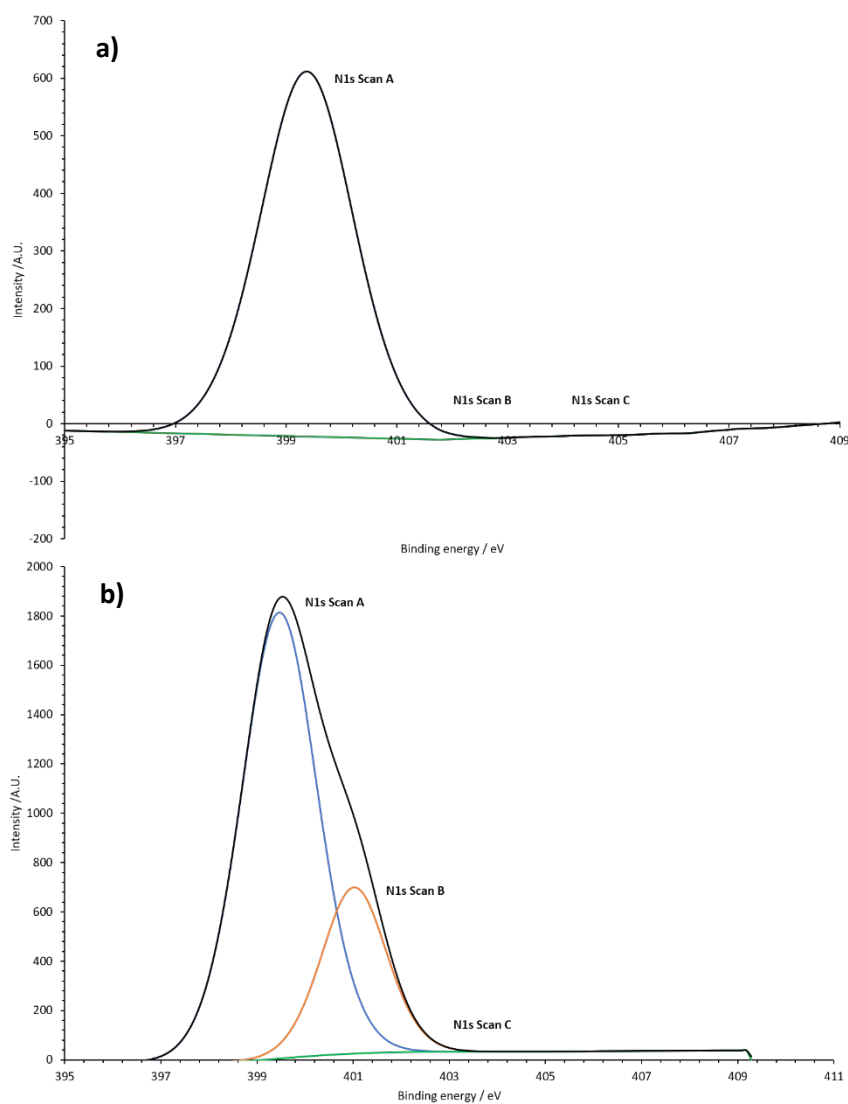

Figure 4. High resolution XPS spectra of peak N1s of samples synthesized with a) CH$_4$O$_3$S and b) HNO$_3$.

3.3. Photoelectrochemical (PEC) analysis

The photoelectrochemical characterization of the WO_3 nanostructures obtained in CH_4O_3S, since they are the ones that have shown the best structural properties, was performed through EIS measurements under light conditions. In order to complement the photoelectrochemical characterization carried out in other studies [25] in this work the charge transfer mechanism at the semiconductor/electrolyte interface upon illuminating the photoanode, has been analyzed. This study was carried out at different applied potentials (versus Ag/AgCl) under AM 1.5 simulated sunlight.

The data obtained with PEIS tests were adjusted to the equivalent electrical circuit presented by Bisquert [26] and the different values associated with both resistances and Constant Phase Element (CPE) elements of the circuit were obtained. To analyze the charge transfer mechanism, the value of the CPE associated with the second R-CPE time constant is needed. Once this value is obtained, using the Brug's expression (equation 2) [27], the capacity value associated with each CPE can be found, to later represent it against the applied potential and analyze the form of the obtained graph [28].

$$C_2 = CPE_2^{\left(\frac{1}{\alpha_2}\right)} \cdot R_2^{\frac{(1-\alpha_2)}{\alpha_2}} \qquad \text{(eq. 2)}$$
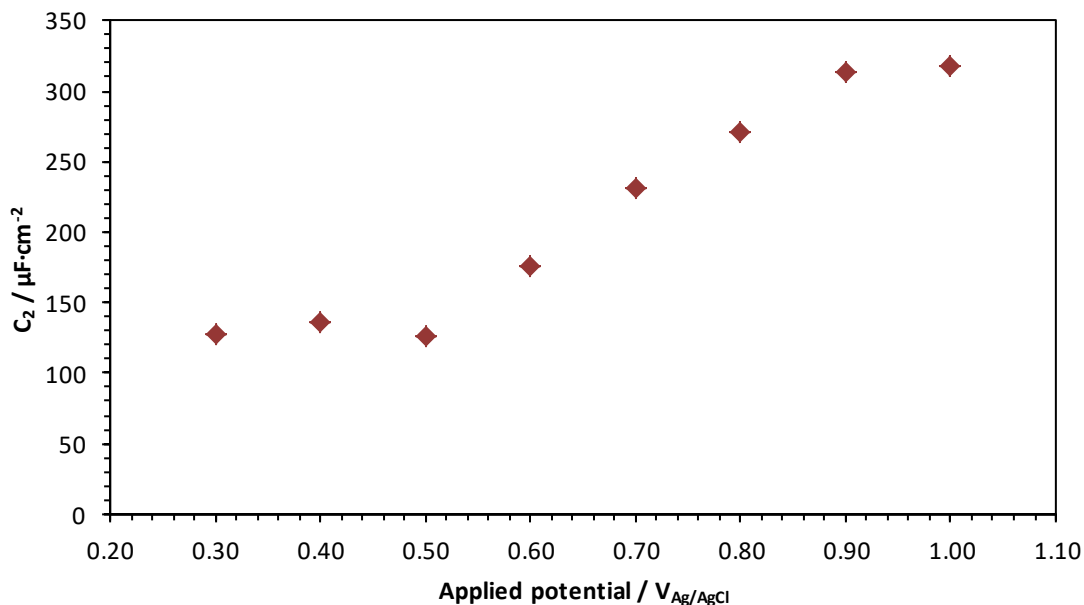
Figure 5. Charge transfer capacitance versus applied potential beyond the flat band potential.

When analyzing Figure 5, it can be concluded that the photo-generated holes are directly extracted from the valence band since the shape of the graph is characteristic of this type of mechanism (resembling an s) according to the theoretical studies performed by Bisquert [26]. In case of being produced from superficial states, the graph would adopt a mountain or peak shape. The fact that the charge transfer of holes takes place via valence band instead of being a process mediated to surface states can be beneficial in the photoelectrochemical behaviour since the recombination of the electron-hole pairs may be reduced, giving a better photoelectrocatalytic efficiency [29,30].

3.4. Photodegradation pesticides (UHPLC-Q-TOF/MS)

The three pesticides mentioned above have been degraded using the nanostructures obtained in CH_4O_3S as electrolyte, which have been the ones that presented the best structural properties in this work, and photoelectrochemically in previous works [31].

The results obtained from the degradation of the three chosen organophosphorus pesticides are shown below. These results have been obtained after analyzing the samples with UHPLC-Q-TOF/MS.

3.4.1. Clorfenvinphos.

First, a calibration curve was obtained after analyzing 4 chlorfenvinphos standards, whose m/z value is 358.9772, using UHPLC-Q-TOF/MS [32–34], in order to obtain the concentrations of pesticide after degradation. Two calibration curves were obtained since two peaks associated with a different enantiomer of the molecule (E (levorotary) and Z (dextrorotary)) appeared in the chromatogram.

The first line corresponds to the enantiomer that appears at a retention time of 20.2 min (eq. 3) and the second to the enantiomer that appears at 21.4 min (eq. 4). Thus, the degradation of each enantiomers can be followed.

$$Area\ (counts) = 366555.02 \times concentration \quad (eq.\ 3)$$

$$Area\ (counts) = 1290695.1 \times concentration \quad (eq.\ 4)$$

In Figure S1 (supplementary material), the Total Ion Chromatogram (TIC) chromatogram of the degraded samples is shown, as well as a magnification of the peaks associated with chlorfenvinphos. This degradation has been carried out for 24 hours, in order to subsequently obtain a complete degradation route.

It can be seen how the concentration of chlorfenvinphos decreased with time until it practically disappeared after 24 hours of testing. Table 1 shows the concentration of each enantiomer of the pesticide in the different samples analyzed.

Table 1. Chlorfenvinphos concentration in each degraded sample.

	Area peak 1	Concentration peak 1 (E) (ppm)	Area peak 2	Concentration peak 2 (Z) (ppm)
1h	5265392.73	14.36	13959456.24	11.81
2h	5037167.08	13.74	13146945	10.18
3h	4682438.64	12.77	12860103.59	9.96
4h	4223297.95	11.52	11986513.59	9.28
5h	3598339.29	9.81	10340218.04	7.01
6h	2742050.91	7.48	5954599.91	4.61
24h	69531.,93	1.89	193730.56	0.15

It can be seen how after 24 hours of degradation, the concentration of the first enantiomer decreased to a concentration below 2 ppm, while the second enantiomer practically disappeared since its concentration was practically zero.

Furthermore, with the concentrations obtained it has been possible to find the degradation kinetics, that is, the velocity with which the pesticide was degraded. In Figure 6 a, the linearization of the data related to the first peak is shown, according to pseudo-first order kinetics, where the Y-axis represents the logarithm of the quotient between the concentration at time *t* and the initial concentration versus time. The adjustment obtained is adequate since the R^2 obtained is greater than 0.99, therefore, it can be stated that the degradation kinetics of chlorfenvinphos is also pseudo-first order. The equation of the line obtained is the one shown in equation 5.

$$\ln(C/C_0) = -0.1354 \cdot t \quad \text{(eq. 5)}$$

Furthermore, Figure 6 b shows the linearization of the data obtained with the second peak. Due to the good fit it can be concluded that it also follows a pseudo-first order degradation kinetics, whose equation is the following:

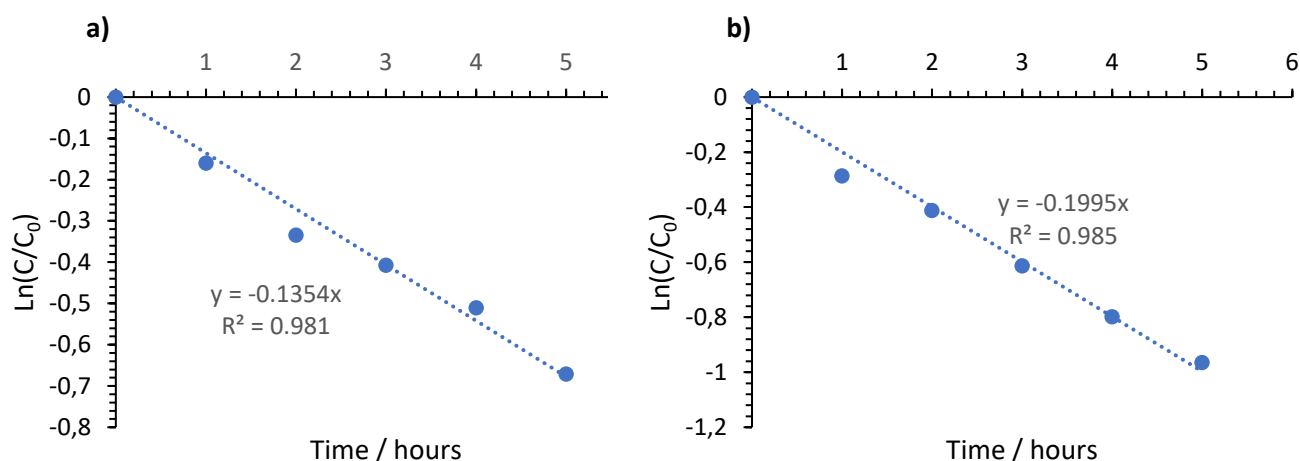$$\ln(C/C_0) = -0.1995 \cdot t \quad \text{(eq. 6)}$$

Figure 6. Pseudo-first order kinetic fit a) first peak (E enantiomer) and b) second peak (Z enantiomer) of chlorfenvinphos samples.

Finally, possible degradation intermediates have been identified during the tests. These intermediates have been identified through bibliography and by analyzing the m/z value of the peaks obtained in the chromatogram of Figure S1 [35].

Therefore, according to the literature, 4 degradation intermediates have been detected, while when analyzing the obtained peaks, 5 more intermediates have been identified.

The proposed degradation pathway for chlorfenvinphos after 24 hours of experiment is shown in Figure 7. It can be seen how the pesticide degrades to give three different routes. On the one hand, the molecule breaks to give the phosphate group (molecule 6 in Figure 7) and the part of aromatic ring (molecule 1 in Figure 7) characteristic of chlorfenvinphos. These two compounds also degrade with time to give smaller molecules. Finally, the third route of degradation of the pesticide was the breakdown of the chlorfenvinphos molecule by the bond

with phosphorus, but in this case, giving rise to a compound without chlorine atoms and with longer aliphatic chains. Both routes end with the opening of the aromatic ring [36].
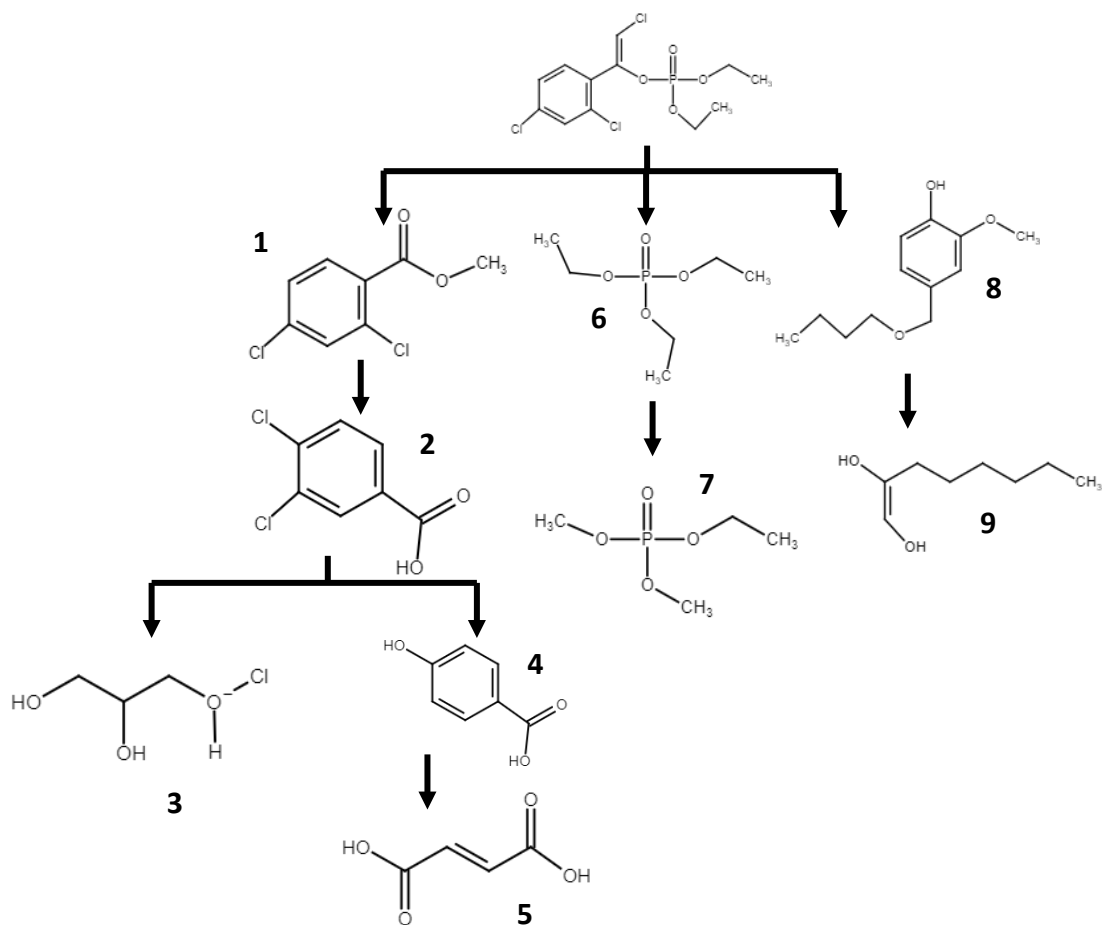

Figure 7. Proposed route of degradation of chlorfenvinphos by PEC.

As a summary, Table 2 shows the molecular formula of each compound, as well as the retention time and the m/z value associated with each intermediate.

Table 2. Summary table of the identified intermediates with their m/z and retention time for chlorfenvinphos.

Compound number	Compound	Molecular formula	Retention time (s)	m/z value
1	2,4- Dichlorobenzoic-methylester acid	$C_8H_8O_2Cl_2$	0.87	203.97
2	2,4- Dichlorobenzoic acid	$C_7H_4O_2Cl_2$	1	189.958
3	1-Chlor-propan-1,2,3-triol	$C_4H_9O_3Cl$	1.04	127.0157
4	4- Hidroxybenzoic acid	$C_7H_6O_3$	0.88	136.9402
5	Dicarboxilic acid	$C_4H_4O_4$	0.95	116.011
6	Trietil phosphate	$C_5H_{13}O_4P$	1.26	182.069
7	Etildimetil phosphate	$C_4H_{11}O_4P$	1.55	155.047
8	4-butoxymetil-2-metoxy-phenol	$C_{12}H_{18}O_3$	9	210.11
9	1-octen-1,2-diol	$C_8H_{16}O_2$	1.37	144.98

3.4.2 Phosmet

The second organophosphorus pesticide chosen to degrade photoelectrochemically has been phosmet, whose m/z value is 318 [37–39].

Four standards were analyzed with the same concentrations as in the previous pesticide to obtain the following calibration curve (eq. 7) :

$$Area \ (counts) = 326844 \times concentration \quad (eq.7)$$

In Figure S2 a) the EIC chromatogram of the degraded samples is shown together with the mass spectrum associated with this peak (Figure S2 b)), which corresponds to the phosmet. It can be observed how after 24 hours of degradation, there is practically no phosmet, producing a 99.9% of pesticide degradation.

Table 3 shows the concentration of phosmet in each solution, found from the calibration curve (eq 7), where it it can be seen that after 24 hours of degradation the concentration of phosmet is zero.

Table 3. Phosmet concentration in each degraded sample.

	Area	Concentration/ ppm
0	6242460.05	19.55
1	4587684.49	14.37
2	3540926.89	11.09
3	2536377.09	7.95
4	1583506.65	4.96
5	1199270.97	3.76
6	499695	1.57
24	10.5	0

According to Figure 8, the degradation kinetics of this pesticide is again adjusted to pseudo-first order kinetics since a good fit has been obtained.
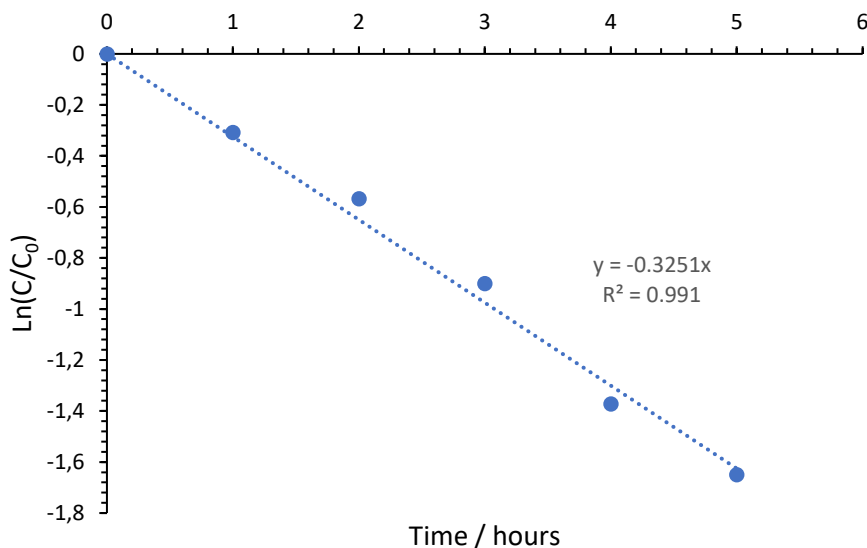
Figure 8. Pseudo-first order kinetic fit of phosmet degradation.

Then, degradation intermediates have been identified and a degradation route has been proposed (Figure 9). It can be observed how in the first place an oxidative desulfurization occurs, where sulfur is replaced by an oxygen atom. This compound is degraded to give compound number 2, where the molecule has been broken by bonding with phosphorus, and sulfur has also been replaced by another oxygen atom. This compound can be degraded to result in compound number 3, where the new compound has lost an OH. And finally, that compound degrades into two possible intermediates (compound 4 and 5 in Figure 9) [11,38].

In addition to this main degradation route, another degradation intermediate (compound 6) has also been identified that would be a direct product of the degradation of phosmet to later degrade into smaller molecules [39–41].
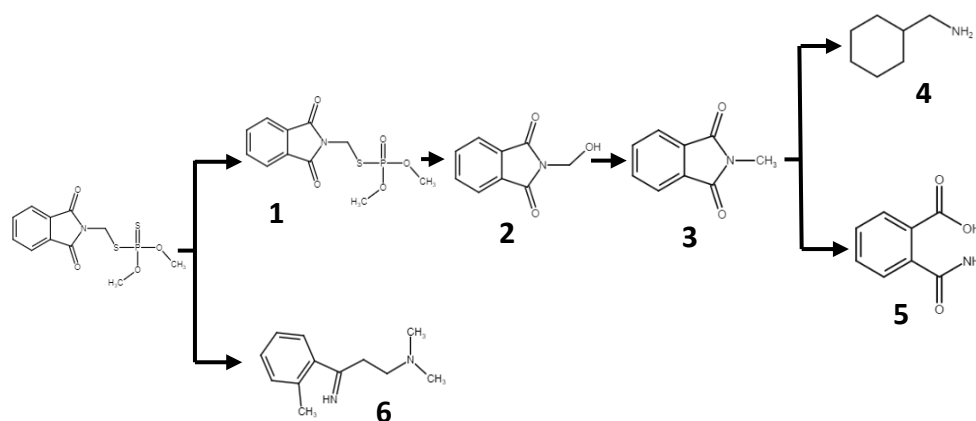
Figure 9. Proposed route of degradation of phosmet by PEC.

As a summary, Table 4 shows the molecular formula, the retention time and the m / z value associated with each intermediate.

Table 4. Summary table of the identified intermediates with their m/z and retention time of phosmet degradation.

Compound number	Compound	Molecular formula	Retention time (s)	m/z value
1	Fosmet-oxon	$C_{11}H_{12}O_5NPS$	13.25	302.025
2	N-Hidroxymethylphthalimide	$C_9H_7NO_3$	2.4	178.05
3	N-Methylphthalimide	$C_9H_7NO_2$	3.85	162.055
4	Cyclohexyl(methyl) amine	$C_7H_{16}N$	1	113
5	Phthalamic acid	$C_8H_7NO_3$	2.1	166.05
6	Dimethyltryptamine	$C_{10}H_{16}N_2$	9.1	188.13

3.4.3. Fenamiphos

Finally, the third pesticide chosen to degrade has been fenamiphos whose m/z value is 304.01 [42–44].

The calibration curve (eq. 8) was obtained to find the concentration of fenamiphos in each degraded sample.

$$Area\ (counts) = 1280777.89 \times concentration \quad \text{(eq.8)}$$

The EIC chromatogram associated with fenamiphos of all the degraded samples, as well as the mass spectrum is represented in Figure S3. It can be seen that after two hours of degradation the concentration of pesticide decreased until 1 ppm approximately. The exact concentration of fenamiphos in each sample is shown in Table 5.

Table 5. Fenamiphos concentration in each degraded sample

	Area	Concentration/ppm
0	24774548.1	19.34
1 h	3691487.39	2.88
2 h	1369919.35	1.07
3 h	706272.27	0.55
4 h	355661.18	0.27
5 h	191351.81	0.14
6 h	97792.98	0.707
24 h	0.46	0

These data have been approximated a pseudo-first order kinetics (Figure 10), as occurs with the two previous pesticides, getting a good fit due to the value of R^2.
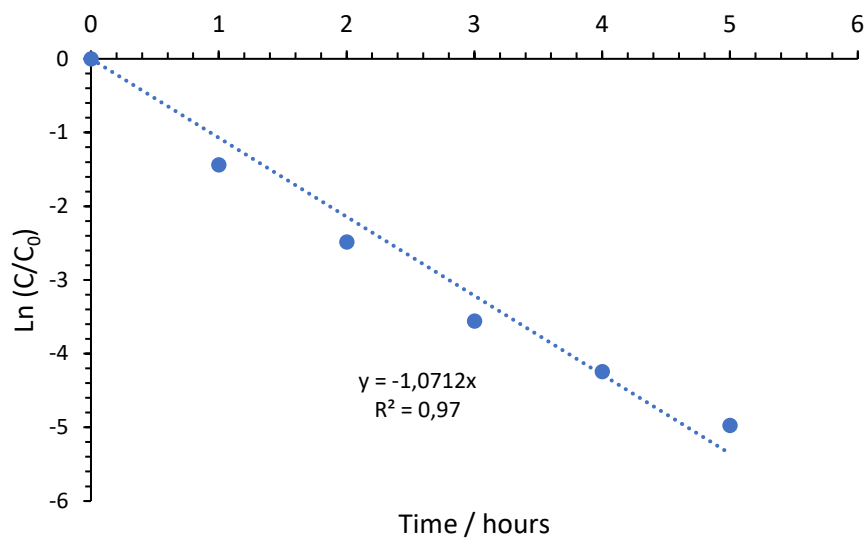
Figure 10. Pseudo-first order kinetic fit of fenamiphos pesticide.

After analyzing the data related to fenamiphos, the possible degradation intermediates produced during 24 hours have been identified. Figure 11 shows the degradation pathway proposed for fenamiphos after analyzing the data obtained by UHPLC-Q-TOF/MS.
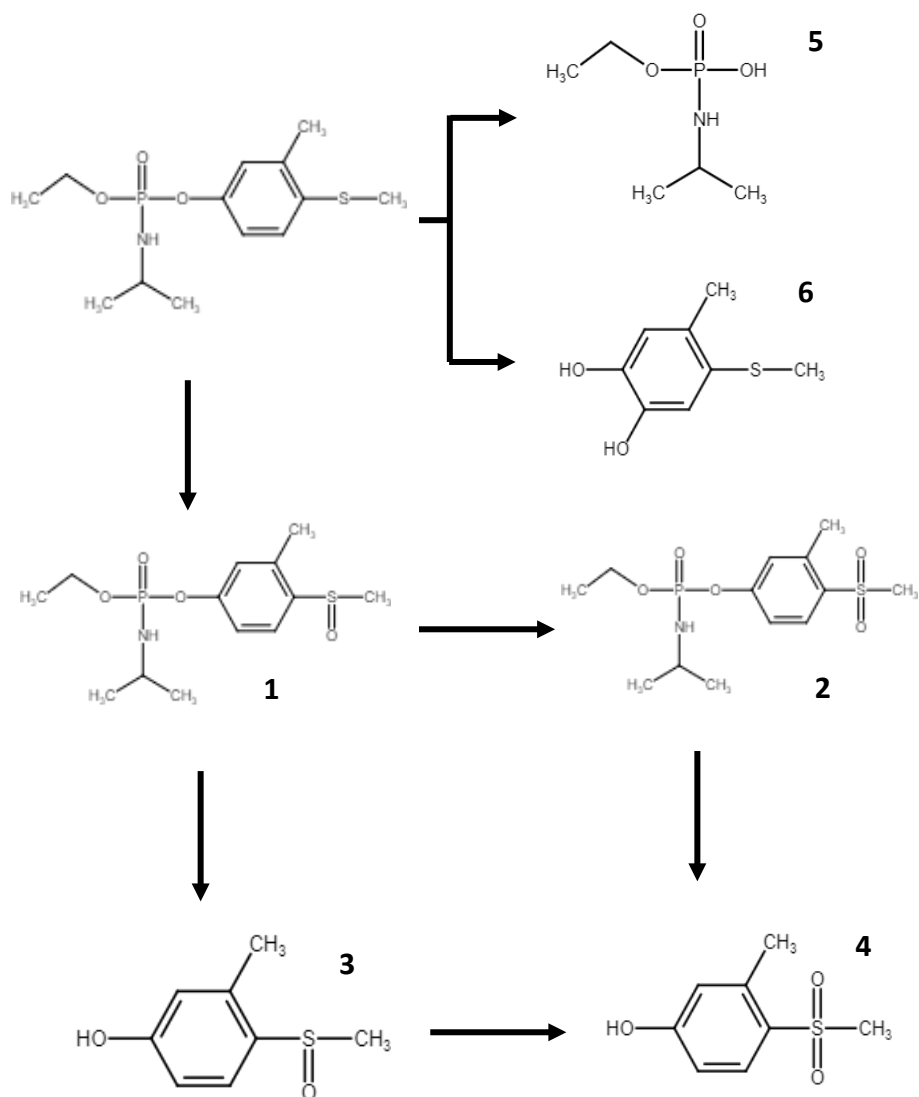
Figure 11. Proposed degradation pathway of fenamiphos by PEC.

This route has two main degradation pathways. The first of them is the formation of the compound fenamiphos sulfoxide (1 in Figure 11) to later degrade and give fenamiphos sulfoxide phenol (3 in Figure 14) and fenamiphos sulfone (2 in Figure 11). Once produced, these intermediate compounds degrade to finally give fenamiphos sulfone phenol (4 in Figure 11) [45–47].

The second degradation route is the formed by the breakdown of the molecule by the P-O bond to give two different molecules (5 and 6 in Figure 11), one of them containing the aromatic ring and the other containing the phosphorus with the rest of the oxygens [48,49].

As a summary, Table 6 shows the molecular formula, retention time, and m/z value of each identified intermediate.

Table 6. Summary table of the identified intermediates with their m/z and retention time of fenamiphos.

Compound number	Compound	Molecular formula	Retention time (s)	m/z value
1	Fenamiphos sulfoxide	$C_{13}H_{22}NO_4PS$	0.8	302.025
2	Fenamiphos sulfone	$C_{13}H_{22}NO_5PS$	5.3	336.10
3	Fenamiphos sulfoxide phenol	$C_8H_{10}SO_2$	0.92	170.04
4	Fenamiphos sulfone phenol	$C_8H_{10}SO_3$	1.4	186.03
5	Ethyl hydrogen isopropyl phosphoramidate	$C_5H_{14}O_3PN$	1.05	168
6	4-methyl-5-(methylthio)benzene-1,2-diol	$C_8H_{10}O_2S$	0.85	171

4. Conclusions.

Once the nanostructures obtained with the different acids have been characterized and the three organophosphate pesticides have been degraded, the following conclusions have been obtained.

According the XRD study, highly crystalline WO_3 monoclinic nanostructures with preferential orientation along the (200) plane were obtained after annealing at 600 ⁰C in an air atmosphere.

Regarding the XPS results, the nanostructures synthesized in CH_4O_3S as electrolyte present a greater number of oxygen vacancies and a greater amount of non-stoichiometric tungsten (WO_{3-x}) than the nanostructures made in H_2SO_4 and HNO_3; thereby resulting in better charge transfer and photoelectrocatalytic behaviour.

Furthermore, the photoelectrochemical study showed that the charge transfer mechanism for photogenerated holes in the WO_3 nanostructures occurs through the valence band, which might be beneficial in order to avoid the recombination between electron-holes at surface states and then, to obtain higher photocurrent densities.

Finally, the three selected pesticides have been degraded using the nanostructures obtained in CH_4O_3S, since they were the ones with the best morphological, structural and photoelectrochemical properties. In case of chlorfenvinphos, it has been possible to degrade up to 90% since the concentration after 24 hours of degradation has been below 2 ppm identifying 9 intermediate compounds. Phosmet has degraded 99% and 6 compounds have been identified, and finally, fenamiphos has been degraded 100% after 24 hours of degradation and another 6 intermediate compounds have been identified, following a pseudo-first order kinetics in all cases. With all of them, a degradation route has been proposed for each compound.

With these results, the excellent behavior of these nanostructures in the degradation of the three selected subfamilies of organophosphorous pesticides is verified, being able to affirm that they are also capable of effectively degrading the rest of pesticides that belong to these subfamilies.

Acknowledgments

References

1.   Bavcon, M.; Trebše, P.; Zupančič-Kralj, L. Investigations of the determination and transformations of diazinon and malathion under environmental conditions using gas chromatography coupled with a flame ionisation detector. *Chemosphere* **2003**, *50*, 595–601, doi:10.1016/S0045-6535(02)00643-4.

2.   Singh, B.K.; Walker, A. Microbial degradation of organophosphorus compounds. *FEMS Microbiol. Rev.* **2006**, *30*, 428–471, doi:10.1111/j.1574-6976.2006.00018.x.

3.   Popoca, C. MECHANISMS AND STRATEGIES FOR PESTICIDE BIODEGRADATION : OPPORTUNITY FOR WASTE , SOILS AND WATER CLEANING de Investigación en Biotecnología , Universidad Autónoma del Estado de Morelos de Gestión Ambiental Universitario , Universidad Autónoma del Estado d. **2013**.

4.   Guivarch, E.; Oturan, N.; Oturan, M.A. Removal of organophosphorus pesticides from water by electrogenerated Fenton's reagent. *Environ. Chem. Lett.* **2003**, *1*, 165–168, doi:10.1007/s10311-003-0029-4.

5.   Oliveira, C.; Alves, A.; Madeira, L.M. Treatment of water networks (waters and deposits) contaminated with chlorfenvinphos by oxidation with Fenton's reagent. *Chem. Eng. J.* **2014**, *241*, 190–199, doi:10.1016/j.cej.2013.12.026.

6.   U.S. Department of Health and Hman Services Toxicological Profile for Chlorfenvinphos. *ATSDR's Toxicol. Profiles* **2002**, doi:10.1201/9781420061888_ch54.

7.   Kuzmanović, M.; Ginebreda, A.; Petrović, M.; Barceló, D. Risk assessment based

prioritization of 200 organic micropollutants in 4 Iberian rivers. *Sci. Total Environ.* **2015**, *503–504*, 289–299, doi:10.1016/j.scitotenv.2014.06.056.

8.   Calatayud-Vernich, P.; Calatayud, F.; Simó, E.; Picó, Y. Occurrence of pesticide residues in Spanish beeswax. *Sci. Total Environ.* **2017**, *605–606*, 745–754, doi:10.1016/j.scitotenv.2017.06.174.

9.   Dorneles, A.L.; de Souza Rosa, A.; Blochtein, B. Toxicity of organophosphorus pesticides to the stingless bees Scaptotrigona bipunctata and Tetragonisca fiebrigi. *Apidologie* **2017**, *48*, 612–620, doi:10.1007/s13592-017-0502-x.

10.   ChemSrc Phosmet properties Available online: https://www.chemsrc.com/en/cas/732-11-6_509792.html (accessed on Apr 24, 2020).

11.   Hernández, F.; Grimalt, S.; Pozo, Ó.J.; Sancho, J. V. Use of ultra-high-pressure liquid chromatography-quadrupole time-of-flight MS to discover the presence of pesticide metabolites in food samples. *J. Sep. Sci.* **2009**, *32*, 2245–2261, doi:10.1002/jssc.200900093.

12.   Cáceres, T.; Ying, G.G.; Kookana, R. Sorption of pesticides used in banana production on soils of Ecuador. *Aust. J. Soil Res.* **2002**, *40*, 1085–1094, doi:10.1071/SR02015.

13.   Cáceres, T.; Megharaj, M.; Venkateswarlu, K.; Sethunathan, N.; Naidu, R. *Fenamiphos and Related Organophosphorus Pesticides : Environmental Fate and Toxicology*; 2010; ISBN 9781441956231.

14.   Upadhyay, S.B.; Mishra, R.K.; Sahay, P.P. Enhanced acetone response in co-precipitated WO3 nanostructures upon indium doping. *Sensors Actuators, B Chem.* **2015**, *209*, 368–376, doi:10.1016/j.snb.2014.11.138.

15.   Huirache Acuña, R.; Lara Romero, J.; Rivera Muñoz, E.M.; Reyes Francis, E.; Franco Casanova, K.M.; García Martínez, I.P.; Castro Cedeño, B.; Paraguay Delgado, F. Síntesis

hidrotérmica de nanoestructuras de óxido de tungsteno (WO3) monoclínico. *Memorias del XXXIV encuentro Nac. y II Congr. Int. la AMIDIQ* **2013**, 2076–21079.

16.   Lethy, K.J.; Beena, D.; Vinod Kumar, R.; Mahadevan Pillai, V.P.; Ganesan, V.; Sathe, V. Structural, optical and morphological studies on laser ablated nanostructured WO 3 thin films. *Appl. Surf. Sci.* **2008**, *254*, 2369–2376, doi:10.1016/j.apsusc.2007.09.068.

17.   Tahir, M.B.; Nabi, G.; Khalid, N.R. Enhanced photocatalytic performance of visible-light active graphene-WO3 nanostructures for hydrogen production. *Mater. Sci. Semicond. Process.* **2018**, *84*, 36–41, doi:10.1016/j.mssp.2018.05.006.

18.   Hatel, R.; Baitoul, M. Nanostructured tungsten trioxide (wo3): Synthesis, structural and morphological investigations. *J. Phys. Conf. Ser.* **2019**, *1292*, 0–5, doi:10.1088/1742-6596/1292/1/012014.

19.   Guo, Y.; Quan, X.; Lu, N.; Zhao, H.; Chen, S. High photocatalytic capability of self-assembled nanoporous WO3 with preferential orientation of (002) planes. *Environ. Sci. Technol.* **2007**, *41*, 4422–4427, doi:10.1021/es062546c.

20.   Huang, Z.F.; Song, J.; Pan, L.; Zhang, X.; Wang, L.; Zou, J.J. Tungsten oxides for photocatalysis, electrochemistry, and phototherapy. *Adv. Mater.* **2015**, *27*, 5309–5327, doi:10.1002/adma.201501217.

21.   Navío, C.; Vallejos, S.; Correig, X.; Bittencourt, C. Gold clusters on WO3 nanoneedles grown via AACVD: XPS and TEM studies. *Mater. Chem. Phys.* **2012**, *134*, 809–813, doi:10.1016/j.matchemphys.2012.03.073.

22.   Shpak, A.P.; Korduban, A.M.; Medvedskij, M.M.; Kandyba, V.O. XPS studies of active elements surface of gas sensors based on WO3-x nanoparticles. *J. Electron Spectros. Relat. Phenomena* **2007**, *156–158*, 172–175, doi:10.1016/j.elspec.2006.12.059.

23.   Wang, L.; Xu, X.; Wu, S.; Cao, F. Nonstoichiometric tungsten oxide residing in a 3D

nitrogen doped carbon matrix, a composite photocatalyst for oxygen vacancy induced

VOC degradation and H2 production. *Catal. Sci. Technol.* **2018**, *8*, 1366–1374,

doi:10.1039/c7cy02572f.

24.   Sadek, A.; Zheng, H.; Breedon, M.; Spizzirri, P.G.; Wlodarski, W.; Kalantar-zadeh, K.

High-temperature anodized WO3 nanoplatelet films for photosensitive devices.

Langmuir **2009**, *25*, 9545–9551, doi:10.1021/la901944x.

25.   Roselló-Márquez, G.; Fernández-Domene, R.M.; Sánchez-Tovar, R.; García-Antón, J.

Influence of annealing conditions on the photoelectrocatalytic performance of WO3

nanostructures. *Sep. Purif. Technol.* **2020**, *238*, 116417,

doi:10.1016/j.seppur.2019.116417.

26.   Bertoluzzi, L.; Lopez-Varo, P.; Jiménez Tejada, J.A.; Bisquert, J. Charge transfer

processes at the semiconductor/electrolyte interface for solar fuel production: Insight

from impedance spectroscopy. *J. Mater. Chem. A* **2016**, *4*, 2873–2879,

doi:10.1039/c5ta03210e.

27.   Brug, G.J.; van den Eeden, A.L.G.; Sluyters-Rehbach, M.; Sluyters, J.H. The analysis of

electrode impedances complicated by the presence of a constant phase element. *J.

Electroanal. Chem.* **1984**, *176*, 275–295, doi:10.1016/S0022-0728(84)80324-1.

28.   Klahr, B.; Gimenez, S.; Fabregat-Santiago, F.; Hamann, T.; Bisquert, J. Water oxidation at

hematite photoelectrodes: The role of surface states. *J. Am. Chem. Soc.* **2012**, *134*,

4294–4302, doi:10.1021/ja210755h.

29.   Cristino, V.; Marinello, S.; Molinari, A.; Caramori, S.; Carli, S.; Boaretto, R.; Argazzi, R.;

Meda, L.; Bignozzi, C.A. Some aspects of the charge transfer dynamics in

nanostructured WO3 films. *J. Mater. Chem. A* **2016**, *4*, 2995–3006,

doi:10.1039/c5ta06887h.

30.   Oskam, G.; Hoffmann, P.M.; Searson, P.C. In situ measurements of interface states at silicon surfaces in fluoride solutions. *Phys. Rev. Lett.* **1996**, *76*, 1521–1524, doi:10.1103/PhysRevLett.76.1521.

31.   Roselló-Márquez, G.; Fernández-Domene, R.M.; Sánchez-Tovar, R.; García-Antón, J. Influence of annealing conditions on the photoelectrocatalytic performance of WO3 nanostructures. *Sep. Purif. Technol.* **2020**, *238*, 116417, doi:10.1016/j.seppur.2019.116417.

32.   Masiá, A.; Ibáñez, M.; Blasco, C.; Sancho, J. V.; Picó, Y.; Hernández, F. Combined use of liquid chromatography triple quadrupole mass spectrometry and liquid chromatography quadrupole time-of-flight mass spectrometry in systematic screening of pesticides and other contaminants in water samples. *Anal. Chim. Acta* **2013**, *761*, 117–127, doi:10.1016/j.aca.2012.11.032.

33.   Luan, J.; Ma, K.; Wang, S.; Hu, Z.; Li, Y.; Pan, B. Research on Photocatalytic Degradation Pathway and Degradation Mechanisms of Organics. *Curr. Org. Chem.* **2010**, *14*, 645–682, doi:10.2174/138527210790963403.

34.   Maldonado, M.I.; Malato, S.; Pérez-Estrada, L.A.; Gernjak, W.; Oller, I.; Doménech, X.; Peral, J. Partial degradation of five pesticides and an industrial pollutant by ozonation in a pilot-plant scale reactor. *J. Hazard. Mater.* **2006**, *138*, 363–369, doi:10.1016/j.jhazmat.2006.05.058.

35.   Portóles, T.; Ibáñez, M.; Sancho, J. V.; López, F.J.; Hernández, F. Combined use of GC-TOF MS and UHPLC-(Q)TOF MS to investigate the presence of nontarget pollutants and their metabolites in a case of honeybee poisoning. *J. Agric. Food Chem.* **2009**, *57*, 4079–4090, doi:10.1021/jf900099u.

36.   M.I. Maldonado Rubio, W. Gernjak, I. Oller Alberola, J. Blanco Gálvez, P. Fernández

Ibáñez, S.M.R. Photo-fenton degradation of alachlor, atrazine, chlorfenvinphos, diuron, isoproturon and pentachlorophenol at solar pilot plant. *Environ. Pollut.* **2006**, *27*, doi:10.1504/IJEP.2006.010459.

37. Vázquez, P.P.; Lozano, A.; Uclés, S.; Ramos, M.M.G.; Fernández-Alba, A.R. A sensitive and efficient method for routine pesticide multiresidue analysis in bee pollen samples using gas and liquid chromatography coupled to tandem mass spectrometry. *J. Chromatogr. A* **2015**, *1426*, 161–173, doi:10.1016/j.chroma.2015.11.081.

38. Baranda, A.B.; Fundazuri, O.; Martínez De Marañón, I. Photodegradation of several triazidic and organophosphorus pesticides in water by pulsed light technology. *J. Photochem. Photobiol. A Chem.* **2014**, *286*, 29–39, doi:10.1016/j.jphotochem.2014.03.015.

39. Kanan, S.M.; Yousef, I.A.A.; Abdo, N.M. The photodecomposition of phosmet over UV irradiated silver nanoclusters doped in mordenite zeolite. *Appl. Catal. B Environ.* **2007**, *74*, 130–136, doi:10.1016/j.apcatb.2007.02.004.

40. Rahman, A.J.; Sharma, D.; Kumar, D.; Pathak, M.; Singh, A.; Kumar, V.; Chawla, R.; Ojha, H. Spectroscopic and molecular modelling study of binding mechanism of bovine serum albumin with phosmet. *Spectrochim. Acta - Part A Mol. Biomol. Spectrosc.* **2021**, *244*, 118803, doi:10.1016/j.saa.2020.118803.

41. European Commission Health & Consumer Protection Conclusion on the peer review of the pesticide risk assessment of the active substance phosmet. *EFSA J.* **2011**, *9*, doi:10.2903/j.efsa.2011.2162.

42. Gao, L.; Qin, D.; Huang, X.; Wu, S.; Chen, Z.; Tang, S.; Wang, P. Determination of pesticides and Pharmaceuticals from Fish Cultivation Water by parallel solid-phase extraction (SPE) and liquid chromatography–quadrupole time-of-flight mass

spectrometry (LC-QTOF-MS). *Anal. Lett.* **2019**, *52*, 983–997, doi:10.1080/00032719.2018.1509076.

43. Ou, L.-T.; Thomas, J.E.; Dickson, D.W. Degradation of Fenamiphos in Soil with a History of Continuous Fenamiphos Applications. *Soil Sci. Soc. Am. J.* **2010**, *58*, 1139, doi:10.2136/sssaj1994.03615995005800040019x.

44. Cáceres, T.; Megharaj, M.; Naidu, R. Degradation of fenamiphos in soils collected from different geographical regions: The influence of soil properties and climatic conditions. *J. Environ. Sci. Heal. - Part B Pestic. Food Contam. Agric. Wastes* **2008**, *43*, 314–322, doi:10.1080/03601230801941659.

45. Herrmann, J.M.; Guillard, C. Photocatalytic degradation of pesticides in agricultural used waters. *Comptes Rendus l'Academie des Sci. - Ser. IIc Chem.* **2000**, *3*, 417–422, doi:10.1016/S1387-1609(00)01137-3.

46. Cáceres, T.; Megharaj, M.; Naidu, R. Toxicity and transformation of fenamiphos and its metabolites by two micro algae Pseudokirchneriella subcapitata and Chlorococcum sp. *Sci. Total Environ.* **2008**, *398*, 53–59, doi:10.1016/j.scitotenv.2008.03.022.

47. Tajeddine, L.; Nemmaoui, M.; Mountacer, H.; Dahchour, A.; Sarakha, M. Photodegradation of fenamiphos on the surface of clays and soils. *Environ. Chem. Lett.* **2010**, *8*, 123–128, doi:10.1007/s10311-008-0198-2.

48. Rai S. Kookana; C. Phang; and L. A. G. Aylmore Transformation and degradation of fenamiphos nematicide and its metabolites in soils. *Aust. J. Soil Res.* **1997**, *35*, 227–239, doi:10.1071/SR96105 0004-9573/97/040753$05.00.

49. Mattern, G.C.; Parker, G.D.; Green, D.L.; Yeutter, G.L. Determination of Phenol Sulfone, Phenol Sulfoxide, and Phenol Sulfonic Acid Metabolites of Fenamiphos in Soil by Liquid Chromatography. *J. AOAC Int.* **1995**, *78*, 1286–1293, doi:10.1093/jaoac/78.5.1286.